agriculture

MDPI

Article

Design and Implementation of an AI-Based Robotic Arm for Strawberry Harvesting

Chung-Liang Chang * and Cheng-Chieh Huang

Department of Biomechatronics Engineering, National Pingtung University of Science and Technology, Neipu, Pingtung 91201, Taiwan

* Correspondence: chungliang@mail.npust.edu.tw; Tel.: +886-8-7703202 (ext. 7586)

Abstract: This study presents the design and implementation of a wire-driven, multi-joint robotic arm equipped with a cutting and gripping mechanism for harvesting delicate strawberries, with the goal of reducing labor and costs. The arm is mounted on a lifting mechanism and linked to a laterally movable module, which is affixed to the tube cultivation shelf. The trained deep learning model can instantly detect strawberries, identify optimal picking points, and estimate the contour area of fruit while the mobile platform is in motion. A two-stage fuzzy logic control (2s-FLC) method is employed to adjust the length of the arm and bending angle, enabling the end of the arm to approach the fruit picking position. The experimental results indicate a 90% accuracy in fruit detection, an 82% success rate in harvesting, and an average picking time of 6.5 s per strawberry, reduced to 5 s without arm recovery time. The performance of the proposed system in harvesting strawberries of different sizes under varying lighting conditions is also statistically analyzed and evaluated in this paper.

Keywords: fruit picking robot; deep learning; visual servoing; fuzzy logic control; hydroponic greenhouse

check for updates

Citation: Chang, C.-L.; Huang, C.-C. Design and Implementation of an AI-Based Robotic Arm for Strawberry Harvesting. *Agriculture* **2024**, *14*, 2057. https://doi.org/10.3390/agriculture14112057

Academic Editor: Jin He

Received: 14 October 2024
Revised: 5 November 2024
Accepted: 13 November 2024
Published: 15 November 2024

Copyright: © 2024 by the authors. Licensee MDPI, Basel, Switzerland. This article is an open access article distributed under the terms and conditions of the Creative Commons Attribution (CC BY) license (https://creativecommons.org/licenses/by/4.0/).

1. Introduction

Farmers are increasingly adopting automated agricultural machinery to improve production efficiency in response to challenges such as unstable crop yields caused by extreme weather, labor shortages, and shrinking available farmland. In recent years, advancements in high-speed computing have matured, and the application of artificial intelligence (AI) in agriculture is now seen as a key future trend. AI has the potential to reduce crop production costs, minimize labor requirements, and even replace manual labor. Notably, mobile automated handling machines and robotic arms integrated with computer vision systems are widely used for highly repetitive tasks like grasping, moving, and placing objects [1]. Unlike industrial robots that function with minimal external interference, agricultural robots must adapt to dynamic outdoor environments to perform tasks such as leaf pruning [2,3], sowing [4], pollination [5], fruit picking [6–10], and transplanting [11]. These rigid robots can withstand higher loads, and their arms are typically designed with multiple axes to enhance workspace flexibility [5]. Some even use dual-arm setups to perform more complex tasks [12]. However, such robots require numerous sensors and actuators, often relying on a ground vehicle for movement to execute tasks. Due to the complexity of positioning control, operations such as pruning, pollination, picking, stem cutting, or fruit suction for individual plants tend to be time-consuming. Although two-degree-of-freedom four-bar robots have been proposed to quickly grasp and place seedling pots on conveyor belts, completing each cycle in approximately 2.25 s on average [11], low-degree-of-freedom mechanisms are more suited for simple transplanting operations. For more complex tasks, like fruit picking, an appropriate control method is essential. Additionally, pneumatic cylinders, suction cups, or soft materials are often used for handling or transporting seedlings. However, for delicate seedlings or mature fruits, improper contact forces can easily cause damage.

A soft arm composed of bio-inspired materials uses fewer actuators to achieve a high degree of freedom [13]. It provides a high degree of flexibility and can be controlled through various methods, including hydro-pneumatic pressure, wire drives, temperature variations, air pressure, and electrorheological or magnetorheological techniques [14–17]. These control methods help reduce operation time and enhance positioning accuracy [10,18,19].

Hofer et al. [20] introduced a spherical soft robotic arm made of fabric, incorporating a spherical pneumatic joint between two arms. The joint is actuated by three actuators, providing two degrees of freedom, and the study analyzes how pressure adjustments in the actuators affect positioning accuracy under different stiffness conditions. Sparrman et al. [16] developed a pneumatic soft robotic arm using silicone, with molds created by 3D printing. The arm comprises hollow silicone wave tubes, where the silicone composition was adjusted to balance rigidity and flexibility, producing an optimal arm that is strong enough to maintain shape, flexible enough to expand and contract, and durable enough to withstand repeated inflation cycles. However, due to the arm's complex structure and highly nonlinear motion, precise positioning and control remain challenging.

On the other hand, for the robotic arm to operate effectively in environments with heavier loads, its material structure must be strengthened. This can be achieved by connecting multiple rigid joints in series to increase its load capacity. When combined with the wire-driven method, the system mimics the contraction of natural tendons. Adding springs or other damping components to support the arm and isolating the drive mechanism from the arm itself can effectively reduce both the size and weight, offering the advantages of a quick response and low latency [21]. Li et al. [22] presented a wire-driven, bio-inspired, multi-jointed robot modeled after the structure and movement of snake-like and continuum robots. Multiple joints replicated the skeleton of a snake, while wire-driven systems imitated the muscles of an octopus's foot. Flexible hoses were inserted into the joints to distribute stress evenly during bending, resulting in smoother movements. This wire-driven approach requires only two to three motors to enable bending in a snake-like robotic arm. Compared to link-based arms, this structure offers significantly higher fault tolerance; even with minor component failures, the system can maintain correct operation [23]. Integrating cable-driven robotic arms of varying sizes can further expand the overall workspace [24]. However, due to the complex movement structure of the arm, accurately estimating and controlling its spatial position remains a considerable challenge [20].

The design of end effectors used in fruit picking directly affects the control methods that follow [25,26]. Common types include gripper claw picking [27], scissor-type cutting [28], and suction [10]. Fan et al. [19] developed a three-fingered rubber gripper, investigating various apple picking methods and comparing the resulting surface damage on the apples. Zhang et al. [10] proposed a vacuum-based apple picking system, where a soft silicone structure conforms closely to the fruit surface to maximize suction efficiency. However, excessive separation force can exert undue strain on the branches, increasing the risk of detaching neighboring fruits. These methods are unsuitable for harvesting delicate fruits like strawberries. Although de Preter et al. [18] improved gripper materials to fully enclose strawberries and reduce surface damage, the picking mechanism still applies a gentle pull and rotational force to separate the calyx, stem, and fruit. In practice, farmers prefer to retain the calyx to minimize the risk of contamination during washing, which remains challenging for current robotic harvesting solutions.

For more fragile fruits like strawberries, a scissor mechanism is designed to cut the fruit stem, while a clamp holds the fruit until the arm reaches the target container, preventing damage to the surface of the strawberry. However, accurately identifying the pedicel cutting point and achieving precise visual positioning control for the robotic arm remains a significant challenge [29].

Machine vision systems are frequently used to assess the state of objects, including their appearance, location, presence of disease, or ripeness. Typically, one or more cameras capture multiple images [30–32], which are then fed into recognition systems to detect target objects and their positions within the image.

Among the diverse object detection methods, image processing and learning-based techniques are the most widely used. Hayashi et al. [33] proposed an image processing method that converts the RGB color space to the hue–saturation–intensity (HSI) color space, allowing the system to determine strawberry ripeness and locate the stem position in the image, achieving a 60% success rate in detecting the target stem. Ge et al. [34] utilized Mask R-CNN along with a refinement method to identify strawberries of varying ripeness, achieving an F1-score of 0.94 for mature strawberries. Sun et al. [35] further integrated a deep learning model with active sensing to detect and locate strawberries. However, as the number of target categories increases, the recognition time also rises, requiring substantial computational resources for real-time picking applications. Although Perez-Borrero et al. [36] developed a strawberry instance segmentation method based on a fully convolutional neural network to improve real-time performance, low accuracy remains a limiting factor, reducing the overall effectiveness of robotic picking.

Utilizing the real-time capabilities and reduced reliance on large datasets of the YOLO (You Only Look Once) architecture, several enhanced methods have proven effective in detecting fruits and their 2D spatial positions [37,38] or in locating stem positions [39]. Furthermore, technologies such as LiDAR, stereo vision, and depth cameras are employed to measure the depth distance of fruits from specific viewpoints [9,40,41], enabling a precise determination of their 3D spatial coordinates. By incorporating additional information on fruit size, scale, and orientation, the 3D position of the stem can be accurately estimated. These data, combined with the robotic arm's kinematic parameters, allow the system to calculate the optimal approach angle and joint movements for effective fruit grasping [40]. Finally, the drive system directs the robotic arm to the target position, enabling it to perform tasks such as spraying or fruit harvesting.

Manually annotating large amounts of data to train recognition models has proven effective in handling complex orchard environments, including variable lighting and fruit diversity (in terms of color, size, and shape). However, most of the existing literature focuses on fruit object recognition in changing environments [42], with little discussion on the performance of robotic arm positioning control. In the application of robotic gripping and control, the arm often requires assistance from contact-based sensors, such as tactile sensors, force sensors, and bending sensors, to perform the operations effectively [43,44]. Fuzzy logic is commonly used to address control issues in uncertain and dynamic conditions within complex scenarios. Originally proposed by Zadeh [45], fuzzy logic is widely applied for precise motor control in agricultural functions such as plowing, sowing, watering, pesticide spraying, and temperature monitoring [46,47]. In 2015, Dimeas et al. [27] developed a fuzzy controller-based gripper with a pressure sensor to adjust grasping force and detect uneven force distribution. This method is often combined with other intelligent control approaches, such as neural networks [48,49]. Subsequently, joint parameters, sensor values, and joint angle variations in the robotic arm are used to build a knowledge base or train the network model. The end effector is driven to the target position through a vision-based servo system and the aforementioned intelligent control methods. However, the picking process still requires considerable time, leaving room for improvement in real-time fruit picking efficiency.

This study presents a precise and stable strawberry picking system designed specifically for handling delicate fruits, overcoming the limitations of existing methods. Unlike the robotic arm joint design in [50], the arm in this study employs multiple ball joints in series, mimicking muscle contractions observed in snake-like movements. This configuration offers enhanced operational flexibility in irregular or variable agricultural environments, surpassing traditional designs that rely solely on rigid structures. Additionally, a two-stage fuzzy logic control system (2s-FLC) is used to precisely control the length of arm and bending angle, significantly improving picking accuracy and simplifying the control complexity compared to conventional systems. Furthermore, unlike traditional gripping or suction-based approaches, the end effector in this system is designed to cut and hold the strawberry stem by clamping only at the stem and base, avoiding direct contact with

the fruit surface. This design effectively minimizes the risk of damage to fragile fruits like strawberries and is rarely seen in the current literature.

This paper is organized as follows: Section 2 outlines the methodology for establishing the fruit picking platform and the process of picking fruits, covering the kinematics of the robot arm, the design of the multi-joint arms and grippers, the fruit picking platform, and the vision-based position control method for the robotic arm. Sections 3 and 4 present the experimental results and discussion. The Section 5 provides the conclusion of the paper.

2. Methodology

This chapter discusses the kinematics of the multi-joint arm, the design and development of the arm and clamps, an outline of the parts of the picking platform, and the position control method for fruit picking. It also details the 2s-FLC method for regulating the motion of robotic arm.

2.1. Motion Model

The robotic arm proposed in this study is composed of multiple joint elements connected in series. The *Y*-axis swinging motion of the three-joint arm in the 2D plane is illustrated in Figure 1. Assuming the length of each joint is represented as l_{n} ($\mathrm{n} = 1, 2, \ldots, N$), N represents the number of joints, and the link length between each joint is equal, with $l_1 = l_2 = \ldots = l$ cm, and the total length of the joint arm is lN. The initial posture of the arm is vertical to the ground. When the arm bends, assuming the bending angle between each joint is equal, $\theta_1 = \theta_2 = \ldots = \theta_N = \theta$, the total bending angle is $\theta_{\mathrm{Total}} = N\theta$. When the displacement at each joint is equal, $\Delta_1 = \Delta_2 = \ldots = \Delta_N = \Delta$, the total displacement is $\ell = N\Delta$. In the 2D plane, assuming the origin of the arm is at coordinate $\mathrm{p}_0(y_0, z_0)$, the coordinates of the n-th joint point $\mathrm{p}_{\mathrm{n}}(y_{\mathrm{n}}, z_{\mathrm{n}})$ when the arm bends are as follows.

$$y_{\mathrm{n}} = y_0 + \sum_{\mathrm{k}=1}^{\mathrm{n}} l \sin(\mathrm{k}-1)\theta \tag{1}$$

$$z_{\mathrm{n}} = z_0 - l - \sum_{\mathrm{k}=1}^{\mathrm{n}} l \cos(\mathrm{k}-1)\theta \tag{2}$$

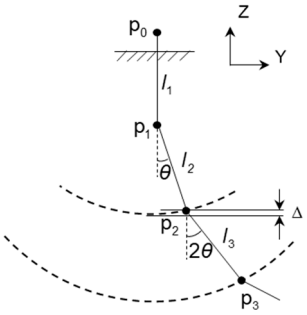

Figure 1. Schematic of joint arm swing (the black dotted line indicates the trajectory of the arm swing).

In this study, the robotic arm can be considered a multi-link structure utilizing spherical joints. The total degrees of freedom of the arm can be calculated using the Chebychev–Grübler–Kutzbach criterion as follows:

$$F = 6(N - 1 - b) - \sum_{j=1}^{b} f_j \tag{3}$$

where b represents the number of joints, and f_j is the number of constrained degrees of freedom for the j-th joint. For spherical joints, each joint constrains 3 degrees of freedom,

allowing 3 rotational degrees of freedom. For example, in a three-link mechanism (with $N = 4$ links, including the base) with $b = 3$ spherical joints, the total degrees of freedom is 9, where $f_j = 3$ for each joint $j = 1, 2, 3$.

2.2. Mechanism and Harvesting Platform

2.2.1. Robot Arm

Several joint components are connected in series to form an arm (Figure 2), which is made up of four tapered spherical components printed using a 3D printer. The sphere of each joint is inserted into the spherical recess on the neighboring joint, allowing it to rotate freely. The root joint of the arm is a level base (upper left in Figure 2), designed for attachment to the motor bracket. Small holes are drilled at the four outer corners of each tapered component, through which four thin wires are threaded. These wires are fastened at the four corners of the terminal joint (bottom left in Figure 2). When the wires are pulled, the arm swings.

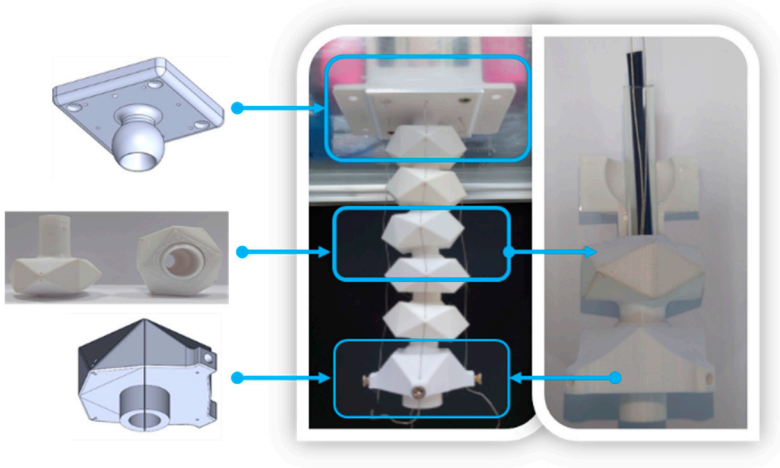

Figure 2. Structure of the multi-jointed robotic arm (**center**); base of the arm (**top left**) and end joint (**bottom left**); internal hoses and thin wires within the arm (**right**).

Additionally, after the joint components are connected in series, a plastic hose is inserted inside the arm (right in Figure 2), ensuring smoother motion during swinging. A thin wire is threaded through the hose, with its end secured to the gripping mechanism at the end of the arm. The driving mechanism adjusts the tension on the wire to open or close the gripping mechanism.

2.2.2. Clamping and Cutting

Two sets of clamping and cutting tools are designed and mounted on the upper and lower sides of the endpoint of arm. This design allows the arm to pick strawberries on the left and right cultivation tubes without needing to rotate, enabling rapid fruit picking. The design concept of the cutter is inspired by the structure of scissors and consists of two blades. Each blade consists of a three-layer structure—top, middle, and bottom (see Figure 3a)—all made of acrylic material. The middle layer contains a trapezoidal groove to hold the blade for cutting strawberry stems, while the top and bottom layers are securely fitted to enclose the blade within the central layer. The ends of the two blades are gear-shaped and meshed together. One end of a thin wire is connected to a round hole at the end of the middle layer of the blade on one side, while the other end is attached to the disk. The center of the disk is coupled to the motor bearing. When the disk is idle, the springs attached to both sides of the clamp keep it in an open position (as shown in Figure 3b). As the disk rotates, the wire is pulled, generating sufficient force to overcome the tension of the springs and bring the two blades together toward the center (as shown in Figure 3c). Figure 3d,e show the physical appearance of the clamping tool and its integration with the

joint arm. When the blades close, the stem is cut and securely gripped, ensuring that the strawberry does not fall (Figure 3f). Additionally, a nozzle is fixed at the center of the joint of arm (bottom left in Figure 3f), connected to a plastic tube, and is used for spraying.

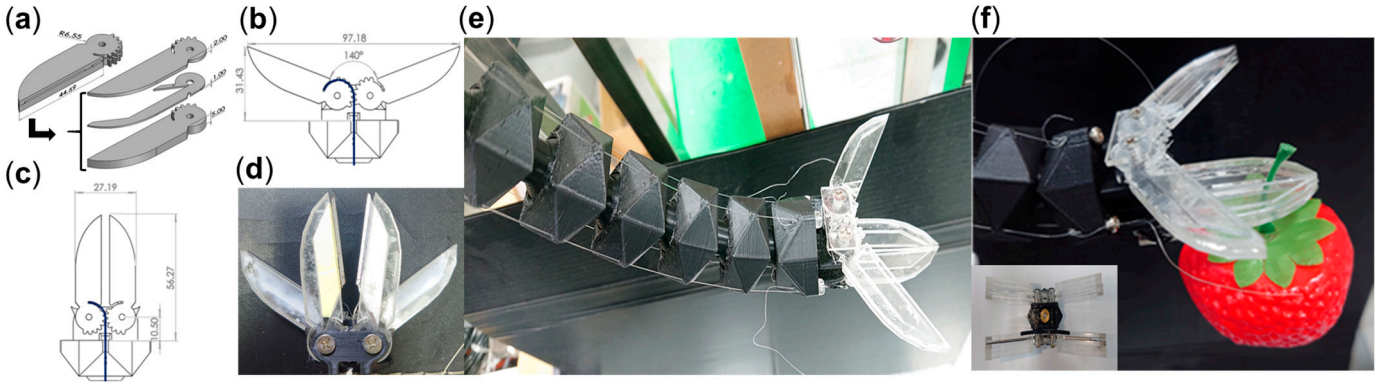

Figure 3. Design of clamp and cutting tool. (**a**) The structure of clamping and cutting tools; (**b**) clamp in the open state; (**c**) clamp in the closed state; (**d**) prototype of the two sets of clamps; (**e**) mounting of the clamp on the joint arm (with the upper clamp in the open state and the lower clamp in the closed state); (**f**) the clamp in action for picking strawberries (the nozzle is installed inside the tube, bottom left).

It is worth noting that in the experiment, the gripper is designed to simultaneously clamp and cut the fruit stem. It securely holds the stem attached to the fruit while avoiding the main plant stem above the blade, ensuring efficient harvesting (see Figure 4). Soft foam lining provides a gentle yet firm grip on the fruit stem.

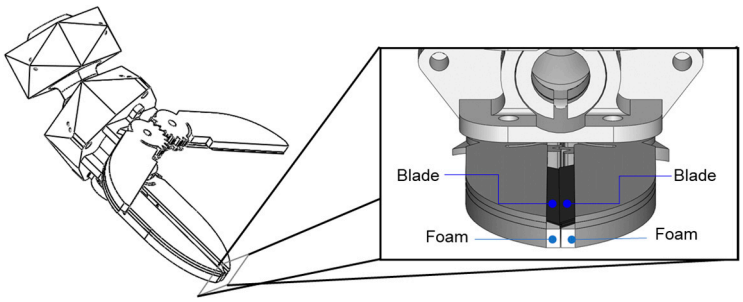

Figure 4. Clamp cutting part with two blades and gripping part with two foam pads.

2.2.3. Platform for Harvesting Strawberries

The robot arm module is mounted on a modified pulley system [51], which moves back and forth along an aluminum extrusion track (Figure 5) on the cultivation support. Two cameras (Model: Brio Ultra 4K HD, Logitech Inc., San Jose, CA, USA) are mounted on either side of the module at a fixed height above the ground to capture images of strawberries on water pipes positioned to the left and right. A microcontroller (Model: Arduino UNO R3, Arduino, Turin, Italy) combined with a sensor expansion board (Model: Sensor Shield V5.0) is used to drive the lifting mechanism within the module (Figure 6). This mechanism includes four built-in servo motors (Model: LD-27MG, Hiwonder Inc., Shenzhen, China): the two lower, symmetrically placed motors are used to regulate the bending angle of the arm, while the two upper motors control vertical arm movement and gripper operation, each connected to a disk wound with thin wire. As the motors rotate, the wire length is adjusted, thereby controlling the arm length, bending angle, and the opening and closing of the clamp.

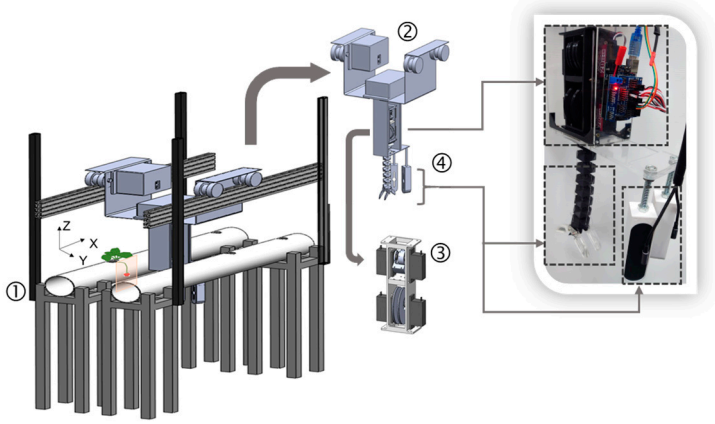

Figure 5. Hydroponic fruit picking platform: ① hydroponic PVC pipe and aluminum extrusion track; ② pulley module; ③ module for raising and lowering the arm; ④ arm with two camera units.

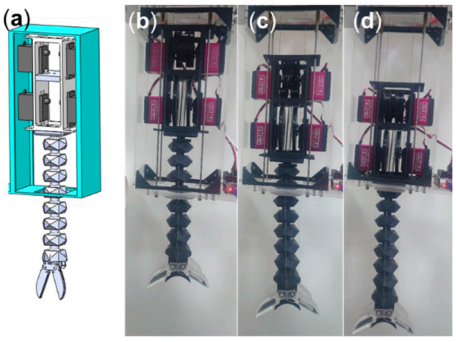

Figure 6. Robotic arm and lifting module: (**a**) prototype of lifting module and mechanism; (**b**–**d**) show the actions of extending the robotic arm.

2.3. Vision-Based Control for Harvesting

This chapter presents the development of the fruit recognition model, the visual positioning control for strawberries, and the lifting and bending mechanisms of the robotic arm.

2.3.1. Fruit Detection and Positioning

The strawberry recognition model is based on YOLOv4, with CSPDarknet53 as its main framework. SPPNet and PANNet architectures are used for feature extraction, and the extracted features are then passed to the Head layer for object detection, loss function calculation, and intersection over union (IoU) evaluation [52].

The process of establishing the strawberry detection model is illustrated in Figure 7. Replica strawberry models, commonly used for landscaping, were selected as picking targets in three sizes: 3.5 cm, 4 cm, and 6 cm (Figure 8). Handheld cameras and experimental cameras were used to capture strawberry objects at different viewing angles. Image augmentation techniques, including scaling, color transformation, affine transformation, and blur processing, were applied to increase the number of images. The dataset was divided into test and validation sets in predetermined ratios, which were used for model training, testing, and verification. Once the model is constructed, it is deployed on the required devices, and its object recognition accuracy is evaluated under different IoU conditions. Once the strawberry within the image is detected and bounded, the inrange() function from the OpenCV library is used to specify a target color to identify the desired object within the bounding box. The cv.contourArea() function is then applied to estimate the total pixel count of the object, representing its contour area, denoted as a. Finally, the circle() function is used to determine the center point of object, indicating the location of the fruit.

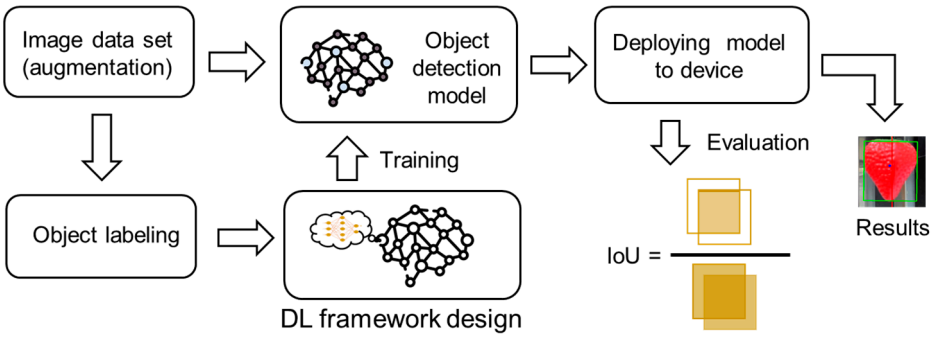

Figure 7. Process of creating the object model.

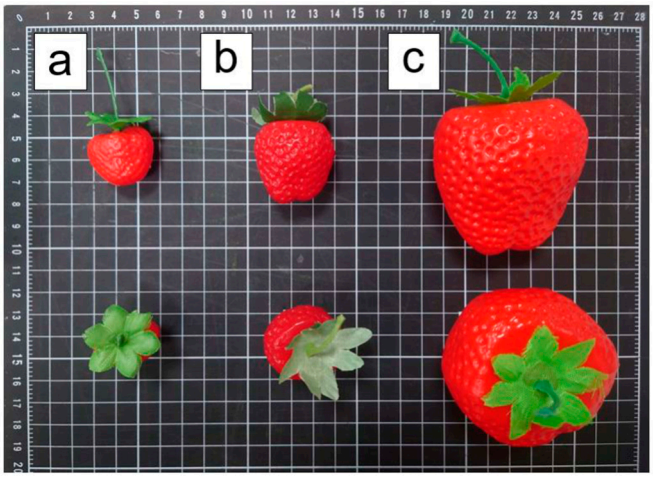

Figure 8. Side view of fruit models in three different sizes, labeled Size 1 (**a**), Size 2 (**b**), and Size 3 (**c**).

The spatial configuration of the joint arm and strawberry is illustrated in Figure 9. The point p_0 represents the arm's origin in the X-Y-Z coordinate frame. Let $o'(x', y', z')$ be the center point of fruit in the X-Y-Z frame, and let its pixel coordinates in the U-V frame, as viewed by the camera, be $\tilde{o}'(u', v')$, where u' and v' indicates the position of fruit along the U-axis and V-axis in pixels, respectively. A movable base, equipped with a vision-based positioning system, adjusts the position of arm along the *X*-axis.

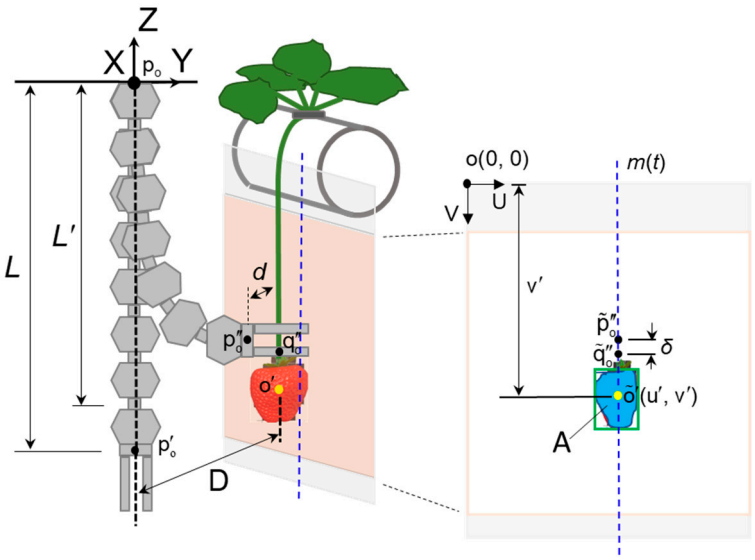

Figure 9. Coordinate configuration of arm and strawberry.

Next, assuming the total length of the joint arm is L and the distance D between the center of fruit and the arm is unknown, the arm must first adjust its length to $\left|L - L'\right|$ for fruit picking operations. L' represents the adjusted length of the arm. The end of the arm should be moved as close as possible to the strawberry while ensuring the initial position of the upper and lower cutting tools at the end of arm remains open to prevent the arm from making contact with the strawberry while bending.

Based on the above conditions and the known strawberry outline area A in the image, a 2s-FLC system is employed to adjust the position $p'_o(x'_o, y'_o, z'_o)$ of the endpoint of arm, guiding it to position p''_o, effectively controlling the joint displacement of arm along the Y-axis and Z-axis. When the arm bends to position p''_o, the lower shearing tool closes, cutting the strawberry stem at point q''_o. The variable δ represents the pixel distance between the cutting point $\widetilde{q}''_o$ in the image and the endpoint of arm $\widetilde{p}''_o$, which is negligible as its value approaches 0. Therefore, the projected distance between point p''_o and the stem can be approximated as $d = \overline{p''_o \widetilde{p}''_o}$. The depth error can be defined as $\eta = \left|d - \hat{d}\right|$, where $\hat{d}$ represents the estimated depth distance.

2.3.2. Lateral (X-Axis) Position Control

The vision-based drive control system moves the platform along the X-axis. Initially, when the platform is stationary ($t = 0$), it is assumed that a line parallel to the image coordinate system and the V-axis in the image captured by the camera is denoted as $m(t) = u$, where the u is a fixed constant corresponding to the position of arm in space. When the center point of frame aligns with this line, the platform will stop, positioning the arm directly with the center of fruit. Let the U-axis value of the center point of object $\widetilde{o}'$ in the image be represented as $u'(t)$. The speed control condition for the platform is as follows:

$$v(t+\Delta t) = \begin{cases} 0 & u = u'(t) \\ v_{max} & u \neq u'(t) \end{cases} \tag{4}$$

$v(t)$ and v_{max} stand for the speed and maximum speed of the moving system at time t. Δt is the sampling time, which includes the time for image processing and updating the speed control commands, and $p_o(t + \Delta t) = p_o(t) + v(t)\Delta t$ is the position of the end point of arm. The speed control goal is to reduce the side displacement error $\varepsilon \rightarrow \min|u - u'|$.

2.3.3. Y- and Z-Axis Position Control

The bending angle of the joints is controlled by four thin wires that pass through holes at opposite corners on both sides of each joint and are secured at the four corners of the end joint. Two of the wires are fixed at the base joint, ensuring the arm swings in a specific direction only. The other two wires are attached to two symmetrical points on a disk driven by a servo motor. As the servo motor rotates, the disk turns, indirectly enabling the winding or unwinding of these two wires, which causes the arm to bend. Assuming the radius of the disk is r, θ_s represents the rotation angle of the servo motor.

$$\theta_s / 180 = \pi r / \ell \tag{5}$$

The picking position of the arm is affected by the fruit's height and size. For strawberries of varying dimensions, even when their center points are at the same height, the arm must adjust both its extension and bending angle to suit each fruit's size. To ensure the end effector reaches close to the target for effective gripping, a 2s-FLC system is implemented to independently control the arm's length and bending angle. The architecture of proposed system is presented in Figure 10.

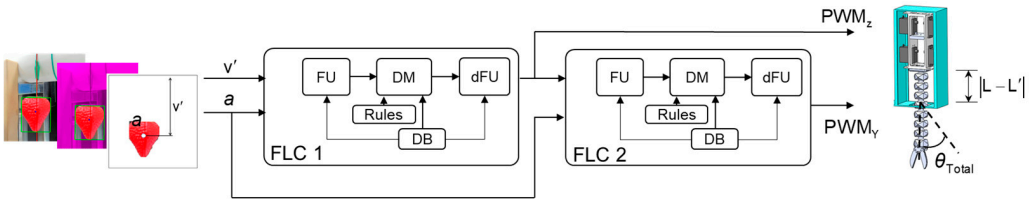

Figure 10. The block diagram of 2s-FLC system.

First, the position $\widetilde{o}'(u', v')$ of the center point of strawberry in the image, its v' value, and the area of strawberry a (in pixels) serve as the input variables for FLC 1, while the pulse width modulation signal PWM_Z is the output variable of FLC 1. This signal drives the servo motor, which rotates the disk and indirectly adjusts the length of the arm, enabling vertical movement along the Z-axis. The PWM_Z value and a are the input variables for FLC 2, with the output variable of FLC 2 being the pulse width modulation signal PWM_Y. This signal drives one servo motor to rotate the disk by an angle θ_s, indirectly adjusting the bending angle of arm θ_{Total}. Since the arm only swings in the Y-axis direction, the other servo motor remains stationary. The internal structure of both controllers includes fuzzification (FU), rules (Rules), decision-making (DM), defuzzification (dFU), and a knowledge base (DB). The design parameters of the 2s-FLC system are listed in Table 1.

Table 1. Illustration of the parameters for 2s-FLC.

Parameters	Description/Value	
	FLC 1	**FLC 2**
Input variables	• v' The length between center point $\widetilde{o}'$ and upper bound of captured image • a: The area of strawberry	• PWM_Z: Pulse width modulation signal (Z-axis) • a: The area of strawberry
Output variables	• PWM_Z: Pulse width modulation signal (Z-axis)	• PWM_Y: Pulse width modulation signal (Y-axis)
Membership functions	Triangular and trapezoidal	
Number of rules	15	15
Inference method	Mamdani	
Defuzzification method	Centroid method	
Performance metrics	• ε: Displacement error • η: Depth error	

A. Fuzzification and knowledge database

Fuzzification is defined as the process of converting the precise numerical values of input or output variables in the controlled system into corresponding fuzzy sets. The input or output variables are defined as the observed values or the control actions applied to the system. During the fuzzification of input variables, fuzzy terms must first be defined, such as 'Big' (B), 'Normal' (N), 'Small' (S), 'Low' (L), 'Medium' (M), 'High' (H), 'Medium Low' (ML), 'Medium Medium' (MM), 'Medium High' (MH), 'High High' (HH), 'High Medium' (HM), 'High Low' (HL), 'Low High' (LH), 'Low Medium' (LM), and 'Low Low' (LL). Each term represents a fuzzy set. Four variables, including v', a, PWM_Z, and PWM_Y, have corresponding fuzzy sets, which may consist of multiple membership functions. Figure 11 shows the triangular and trapezoidal membership functions, the number of functions, and their distribution used for fuzzifying the input and output variables in FLC 1 and FLC 2. The membership function distributions for input variables v' and a of the FLC 1 are shown in Figure 11a and Figure 11b, respectively. Input variable a also serves as the input

for FLC 2. The distributions of membership functions of output variable PWM_Z of FLC 1 is also shown in Figure 11c. Figure 11d,e illustrate the distribution of the five and nine membership functions for input variable PWM_Z of FLC 2 and output variable PWM_Y of FLC 2, respectively. During the fuzzification process, the variable corresponds to multiple fuzzy sets and the degree of membership to each set. For example, if the input variable v′ in FLC 1 is 800 pixels, its membership degrees for 'H', 'MH', 'M', 'ML', and 'L' are 0, 0, 0.28, 0.72, and 0, respectively (Figure 11a). On the other hand, if the fruit area is 1×10^5 pixels, its membership degrees for 'S', 'N', and 'B' are 0, 0.43, and 0.58, respectively (Figure 11b). Another example, if PWM_Z = 2000, the membership degrees for 'LH', 'LM', 'LL', 'ML', 'MM', 'MH', 'HH', 'HM', and 'HL' are 0, 0, 0, 0, 0, 0.2, 0.8, 0, and 0, respectively (Figure 11c).

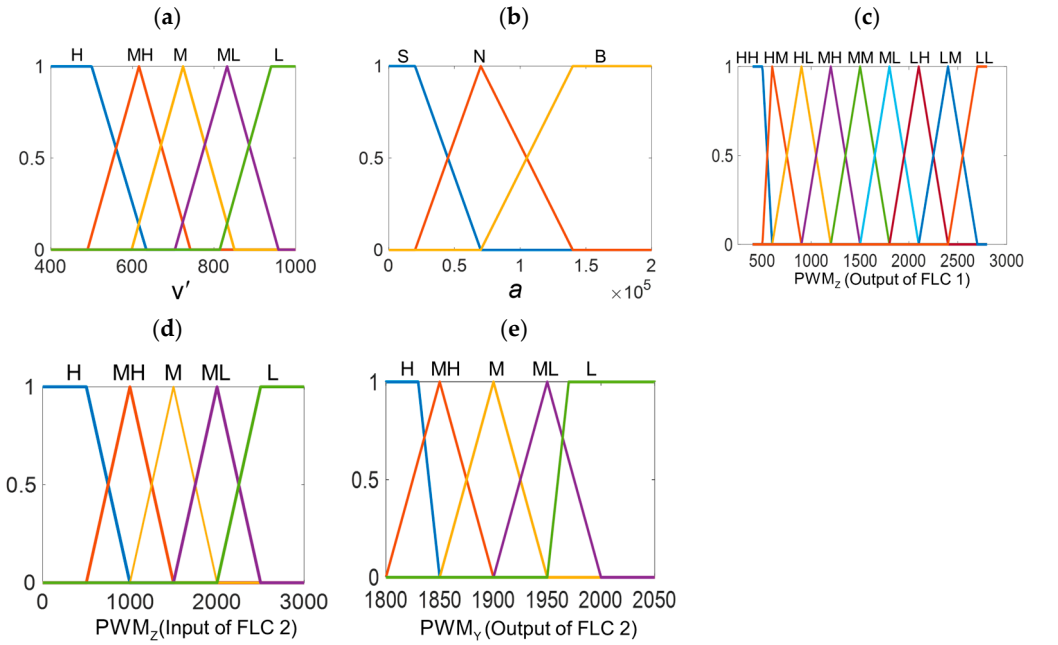

Figure 11. Input and output variable fuzzification for FLC 1 and FLC 2. (**a**) v′ for input of FLC 1; (**b**) *a* for input of FLC 1 and FLC 2; (**c**) PWM_Z for output of FLC 1; (**d**) PWM_Z for input of FLC 2; (**e**) PWM_Y for output of FLC 2.

B. Rules, decision-making, and defuzzification

Rules are formulated based on expert knowledge and are used for inference and decision-making. In FLC 1, a total of 15 rules are established, with each rule expressed in the 'IF-THEN' format.

(1) IF (v′ is H) AND (*a* is B) THEN (PWM_Z is HH)
(2) IF (v′ is H) AND (*a* is N) THEN (PWM_Z is HH)
(3) IF (v′ is H) AND (*a* is S) THEN (PWM_Z is HM)
(4) IF (v′ is MH) AND (*a* is B) THEN (PWM_Z is HL)
(5) IF (v′ is MH) AND (*a* is N) THEN (PWM_Z is HL)
(6) IF (v′ s MH) AND (*a* is S) THEN (PWM_Z is HL)
(7) IF (v′ is M) AND (*a* is B) THEN (PWM_Z is MH)
(8) IF (v′ is M) AND (*a* is N) THEN (PWM_Z is MM)
(9) IF (v′ is M) AND (*a* is S) THEN (PWM_Z is MM)
(10) IF (v′ is ML) AND (*a* is B) THEN (PWM_Z is ML)
(11) IF (v′ is ML) AND (*a* is N) THEN (PWM_Z is LH)
(12) IF (v′ is ML) AND (*a* is S) THEN (PWM_Z is LH)
(13) IF (v′ is L) AND (*a* is B) THEN (PWM_Z is LM)
(14) IF (v′ is L) AND (*a* is N) THEN (PWM_Z is LM)
(15) IF (v′ is L) AND (*a* is S) THEN (PWM_Z is LL)

Similarly, in FLC 2, a total of 15 rules are established, as detailed below.

(1) IF (PWM_Z is H) AND (a is B) THEN (PWM_Y is H)
(2) IF (PWM_Z is H) AND (a is N) THEN (PWM_Y is H)
(3) IF (PWM_Z is H) AND (a is S) THEN (PWM_Y is H)
(4) IF (PWM_Z is MH) AND (a is B) THEN (PWM_Y is MH)
(5) IF (PWM_Z is MH) AND (a is N) THEN (PWM_Y is MH)
(6) IF (PWM_Z is MH) AND (a is S) THEN (PWM_Y is MH)
(7) IF (PWM_Z is M) AND (a is B) THEN (PWM_Y is M)
(8) IF (PWM_Z is M) AND (a is N) THEN (PWM_Y is M)
(9) IF (PWM_Z is M) AND (a is S) THEN (PWM_Y is M)
(10) IF (PWM_Z is ML) AND (a is B) THEN (PWM_Y is ML)
(11) IF (PWM_Z is ML) AND (a is N) THEN (PWM_Y is ML)
(12) IF (PWM_Z is ML) AND (a is S) THEN (PWM_Y is ML)
(13) IF (PWM_Z is L) AND (a is B) THEN (PWM_Y is L)
(14) IF (PWM_Z is L) AND (a is N) THEN (PWM_Y is L)
(15) IF (PWM_Z is L) AND (a is S) THEN (PWM_Y is L)

The Mamdani method is used for fuzzy inference. It involves converting two sets of input values into corresponding fuzzy sets. Each rule is then applied to the inputs, and the membership degree of each fuzzy set is obtained. These sets are then intersected, and the result corresponds to an output fuzzy set (as shown in the blue area on the right side of Figure 12). The output fuzzy sets of all rules are then aggregated using a union operation, forming a single geometric shape (as shown in the blue area at the bottom right). Finally, the centroid method is used to convert the fuzzy output set into a specific value (represented by the thick red line). Additionally, by observing the pattern of the fuzzy inference surface, the suitability of the inference rules can be evaluated, and the rules can be adjusted if necessary to modify the initial inference surface (Figure 13).

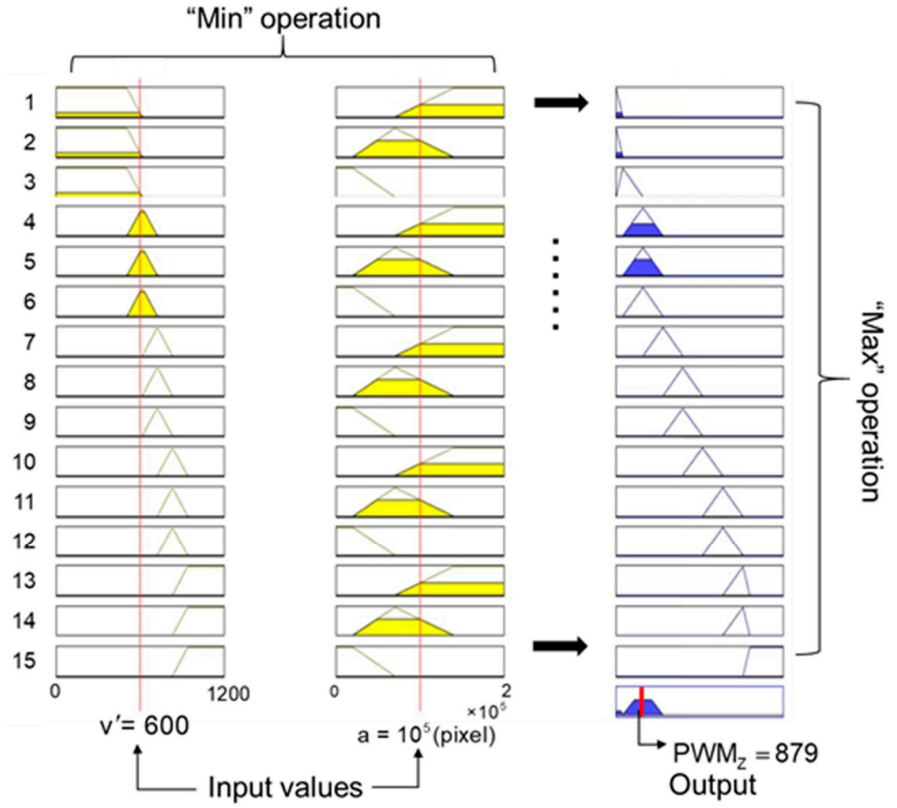

Figure 12. Example of fuzzy inference and defuzzification; fuzzy inference results when v′ = 600 and $a = 10^5$(pixel) (FLC 1).

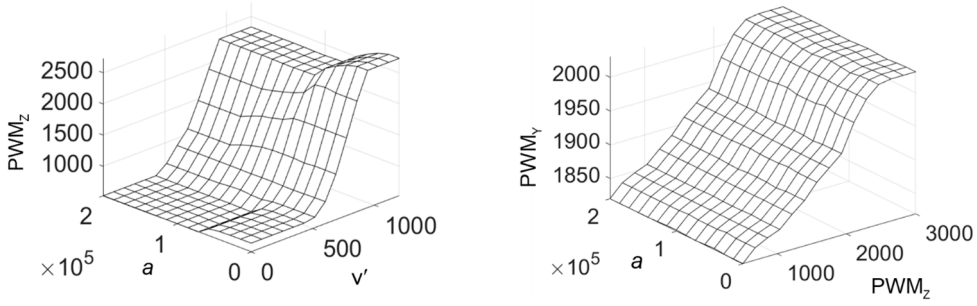

Figure 13. Fuzzy inference surfaces of FLC 1 (**left**) and FLC 2 (**right**).

3. Performance Analysis and Results

This section presents the performance results of the system used to control the joint arm for fruit grasping, focusing on lateral movement control and the positioning accuracy achieved through a 2s-FLC system. Finally, the fruit-grasping experiments were conducted in a greenhouse, where the picking performance of the robotic arm was evaluated under different weather conditions.

3.1. Object Detection

The image dataset consists of 2000 images, with 1400 used for training, 400 for validation, and 100 for testing. The required image sizes for the model during training are 416 × 416 pixels. The training parameters are as follows: batch size set to 16, 200 epochs, and the model is optimized using SGD with a learning rate of 0.0001. The number of iterations is set to 6000, and the loss function, comprising classification loss, localization loss, confidence loss, and object classification loss, is evaluated after each iteration [52]. Next, tissues were twisted into thin strips, dyed green to resemble stems, and tied to the tops of fruit models of different sizes (to the left of Figure 14). These fruit replicas were then randomly suspended along the side of the hydroponic pipe. The identification results are shown in Figure 14 (right), where, with an F1-score of 0.94, a precision of over 88% was achieved.

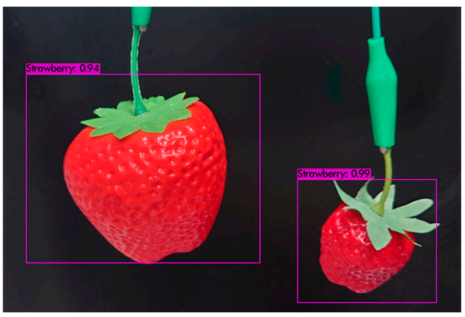

Figure 14. Strawberry identification results.

3.2. Positioning Accuracy

3.2.1. Range of Motion

The Simulink R2022a software tool was used to develop a bending model of the joint arm and simulate its bending behavior [53], resulting in a smooth bending curve (Figure 15a). However, in the actual arm bending test, if the plastic tube is not placed in the intra-arm channel, the bending is irregular (Figure 15b). When the tube is inserted, the joint arm's bending closely matches the simulation results (Figure 15c). The swing trajectory of the arm reveals a clear difference between the cases where the tube is absent and when it is inserted into the joint channel (Figure 16a). The red line represents the arm's movement without the tube, while the blue line shows the trajectory with the tube. Swing trajectories for arms of different lengths are shown in Figure 16b, indicating that the maximum swing range reaches approximately 20 cm.

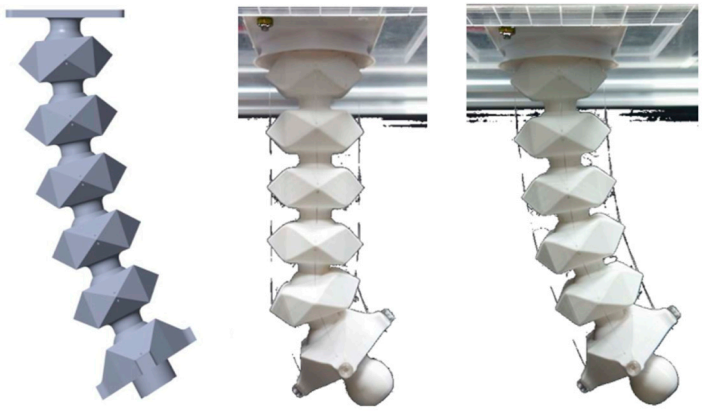

(**a**) (**b**) (**c**)

Figure 15. Bending test of the jointed arm. (**a**) Simulated joint arm bending using the Simulink tool, (**b**) arm bending without the plastic tube inserted, and (**c**) arm bending with the plastic tube inserted.

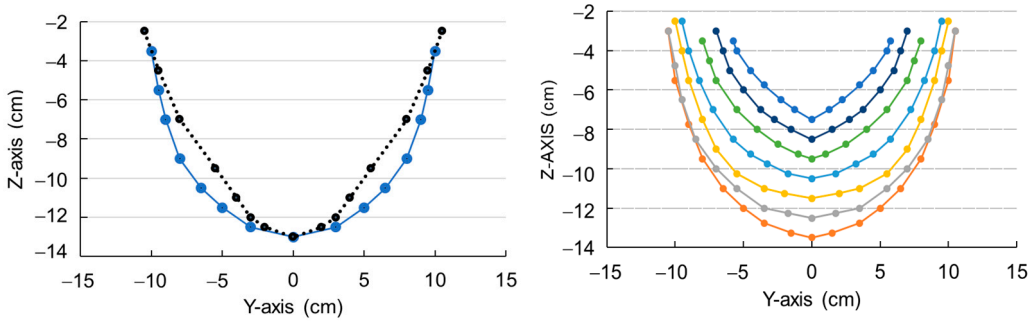

(**a**) (**b**)

Figure 16. Swing trajectory of the joint arm. (**a**) Bending trajectories of PVC plastic pipes with insertion (blue line) and without insertion (black dashed line); (**b**) Relationship between joint arm lengths and swing trajectories (each color represents the swing trajectory for a different joint arm length).

3.2.2. Lateral and Depth Error

In the fruit picking experiment, metrics such as displacement deviations ε, η, FPR, and FDR were used to evaluate the object grasping performance of the fruit picking platform. The Scikit-fuzzy toolkit was used to implement control of the *Z*-axis and *Y*-axis displacement and the bending angle of the robotic arm. The operation process was divided into three stages: platform stopping, arm bending, and gripper picking. First, we observed whether the platform could align the robotic arm with the strawberry replica in the grasping direction. Each size of the strawberry replica was tested five times. The results showed that the average displacement deviations for Size 1, Size 2, and Size 3 objects were 2 mm, 1.4 mm, and 0.8 mm, respectively.

A tissue was rolled into thin strips, dyed green to resemble stems, and then attached to the tops of fruit models of various sizes. Next, using three different fruit sizes, each fruit model was suspended at five random positions. Under the assumed conditions, we observed the distance d between the end position p_o'' of the robotic arm after bending the fruit stem. Additionally, the expected values for this distance were set based on the volumes of Size 1, Size 2, and Size 3, assumed to be 10 mm, 15 mm, and 30 mm, respectively. Ideally, the value of d matches the expected value. Manual measurement is used to obtain d. Table 2 presents a comparison of the average error values obtained using linear control and 2s-FLC. The results also show that using the 2s-FLC method achieves lower error values. In addition, the process of successfully picking a single fruit was observed, and the time taken for each step was recorded, including arm lifting, bending and adjustment, clamping and cutting, lowering the arm, opening the clamp, and returning to the arm origin. Bending

and adjusting the arm took the longest, averaging about 1.9 s (Figure 17), followed by arm lifting, which averaged 1.5 s. The clamping and cutting, along with opening the clamp, required the shortest time, averaging about 0.5 s. The overall average time to pick a single fruit was 6.5 s. Excluding the arm's reset time, the average picking time per fruit is reduced to 5 s.

Table 2. Depth error η between the gripper and the target using a linear control method and a 2s-FLC method, respectively.

Fruit	Test 1	Test 2	Test 3	Test 4	Test 5	Average Error (mm)
Size 1	28.0/24.0 [z]	25.0/20.0	31.0/30.0	29.0/27.0	28.0/29.0	28.2/26.0
Size 2	19.0/19.0	20.0/14.0	19.0/16.0	17.0/13.0	15.0/11.0	18.0/14.6
Size 3	9.0/9.0	6.0/4.0	11.0/13.0	12.0/6.0	10.0/7.0	9.6/7.8

[z]: Linear control/2s-FLC.

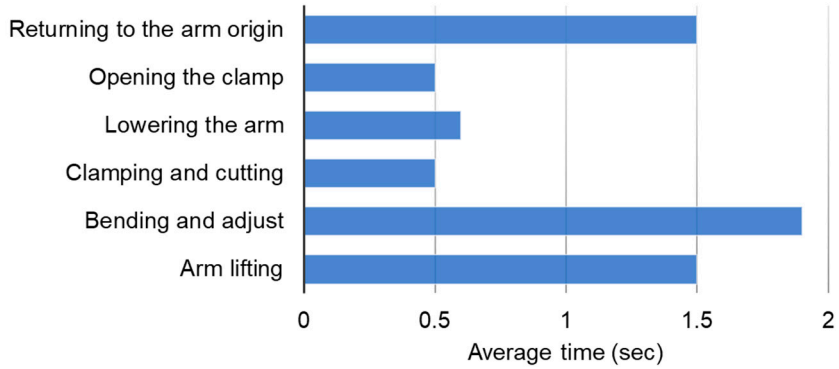

Figure 17. Average time per fruit for single fruit picking operation.

Using three different fruit sizes randomly placed at five locations, the performance of the gripper in grasping the fruit pedicel was tested. The results were categorized as 'successful picking', 'dropped after picking', or 'failed picking'. Table 3 illustrates the findings. Importantly, in Test 4 of the treatments, successful picking results were achieved for all three fruit sizes, with the observed positions of the fruits consistently located toward the lower central area of the image frame.

Table 3. Test results of fruit picking by grippers.

Size of Fruit	Treatments				
	Test 1	Test 2	Test 3	Test 4	Test 5
Size 1	△	●	×	●	×
Size 2	△	●	●	●	●
Size 3	●	×	●	●	△

●: successful picking. △: dropped after picking. ×: failed picking.

3.3. Environmental Condition and Results

The trained model was then deployed to the embedded development board (Model: Jetson NANO, NVIDIA Co., Santa Clara, CA, USA) located on the side of the lifting module. Five fruits of Size 1, Size 2, and Size 3 were randomly suspended on one side of the hydroponic pipe. The platform moved at a speed of 10 cm/s, as shown in Figure 18, with the hydroponic pipe measuring 3.5 m in length. The experiment lasted for three days under mostly cloudy weather. The test period ran from 10:00 AM to 4:00 PM, with the mobile module moving from one end of the pipe to the other once every hour. During the movement, a single camera continuously captured images at 10 frames per second (fps) while the identification system detected strawberries in the images. A total of 2450 images

were collected per day. Three evaluation metrics, including Precision, Recall, and Average Precision (AP), were used to assess the identification performance of deep learning model.

Figure 18. Snapshot of the experimental site (strawberry models of different sizes hung on one side).

The average identification performance of the detection model during each time period over three days is shown in Figure 19. The average precision, recall, AP@0.5, and AP@0.5:0.05:0.95 were 0.891, 0.880, 0.891, and 0.718, respectively. AP@0.5:0.05:0.95 represents the average AP value calculated at IoU thresholds ranging from 0.5, 0.55, . . ., up to 0.95.

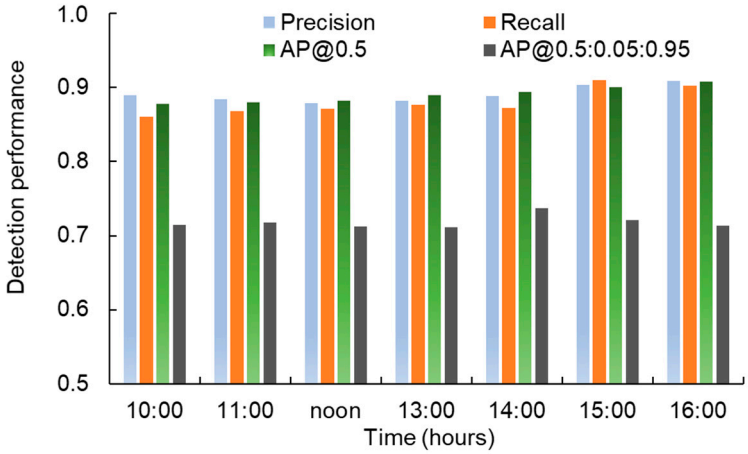

Figure 19. Performance comparison of the detection model at various times.

The fruit picking experiment for this platform was conducted in an outdoor greenhouse at various time intervals and under different weather conditions (longitude: 120°60′61.30″ E; latitude: 22°64′65.96″ N) during the summer of 2023. First, on sunny days, three periods were selected for testing: early morning (5:00−7:00), mid-morning (9:00−11:00), and late afternoon (16:00−18:00). Strawberry replicas were positioned along the sides of the hydroponic pipes (Figure 20). During the early morning and mid-morning sessions, picking was carried out on one side only, while both sides were tested in the late afternoon. For the single-sided experiment, 10 strawberry replicas were hung on one side of the pipe, and for the double-sided experiment, 9 replicas were hung on each side, totaling 18. The stems of the strawberry replicas were tied with thin plastic strings that break easily. The results of fruit picking and positioning are shown in Table 4. The camera images were evenly divided into upper, middle, and lower sections, representing the regions where the

fruit was successfully picked. Figure 21 shows a side view of the operator continuously picking two fruits using the system.

Figure 20. Strawberry picking experiment site (with strawberry models of different sizes hanging on both sides).

Table 4. Test results of fruit picking (single day).

Time Slots	Fruit Location	Number of Fruits	Number of Picked Fruits	Size of Fruits			Location of Fruit		
				Size 1	Size 2	Size 3	Upper	Medium	Lower
05–07	One side	10	6	1	3	2	1	2	3
09–11	One side	10	7	0	4	3	0	4	3
16–18	Double side	18	6	1	2	3	1	4	1

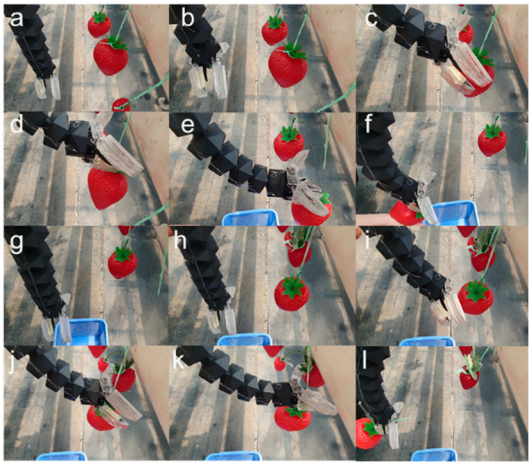

Figure 21. Snapshots of the joint arm grasping a strawberry. (**a**) The joint arm is lowered and aligned with the target; (**b**) the joint arm rises; (**c**) the joint arm bends; (**d**) the gripper cuts the stem; (**e**) the gripper clamps the stem; (**f**) the arm is lowered; (**g**) the gripper releases the stem; (**h**) the mobile platform moves to the next target. Images (**i**–**l**) respectively illustrate the lifting and bending of arm toward the strawberry stem (**i**,**j**), the gripping action (**k**), and finally the arm in a lowered position (**l**).

Finally, the experiment was repeated three times, and both the fruit picking success rate (FPR) and the fruit drop rate (FDR) after grasping were measured. The standard for successful picking is that the arm bends and the gripper securely grasps the fruit until the arm returns to its original position. In contrast, the fruit drop rates show that during the process, the arm either fails to grasp the fruit or the fruit drops mid-operation. As shown in

Table 5, the FPR reached up to 82%. The lowest success rate, only 32%, occurred between 5 and 7 AM under cloudy conditions. Interestingly, under cloudy conditions and near evening, there was no fruit drop at all.

Table 5. Fruit picking success rate.

Time / Weather	Early Morning (05:00−07:00)		Morning (09:00−11:00)		Late Afternoon (16:00−18:00)	
	FPR (%)	FDR (%)	FPR (%)	FDR (%)	FPR (%)	FDR (%)
Sunny	82	18	64	27	55	9
Partly cloudy	55	36	73	18	55	27
Cloudy	37	9	46	18	37	0

4. Discussion

The success rate of fruit picking depends on the accurate identification of the center of the fruit. We observed that the highest success rate occurs during bright early mornings (5−7 AM). In contrast, during overcast mornings or in the late afternoon (4−6 PM) under cloudy skies, the success rate significantly decreases. The light intensity during these periods is relatively low, leading us to infer that weak lighting prevents precise object detection. This result is consistent with earlier research findings [54].

In the experiment, the object detection system operated at 10 fps to perform strawberry identification and estimate the fruit area. However, signal transmission delays between the microcontroller and peripheral devices, at times, led to excessive lateral positioning errors in the mobile platform. This misalignment caused the strawberry stem to deviate significantly from the intended picking position, preventing the cutting tool from effectively cutting the stem. Higher-performance graphic processing units (GPUs) and controllers can execute complex deep learning and image processing algorithms more efficiently, which would improve the performance of the object detection system [55]. The most time-consuming operation of the proposed system is the adjustment of the bending angle of the arm and the picking position, which takes approximately 1.9 s. Using a more advanced processor would help reduce picking time, enhance the system's tolerance for positional errors, and reduce the chance of significant lateral misalignment.

On the other hand, once the harvesting system detects the center point of the target, the platform halts, adjusting the length of the arm and bending angle. However, slight shaking or instability during operation can easily cause the fruit to drop. Furthermore, variations in the placement and height of the water pipe shelf relative to the ground may prevent the robotic arm from precisely aligning with the fruit stem. The flexibility of the wire also influences harvesting accuracy. During experiments, continuous wire tensioning altered its length, causing the end of the arm to miss the intended position. Furthermore, as the arm bends, the wire lengths on the inner and outer sides of the joints vary. This slack can cause the wire to slip out of the rotating shaft groove, leading to it coming off the shaft. Finally, when the gripper at the end of the arm tries to grab the fruit, it sometimes fails to cut the stem. This happens when the stem is near the edge of the gripper, where the cutting force is too weak. The experimental results demonstrate that the wire-driven joint arm offers excellent flexibility in precise position control. However, maintaining consistent tension on the wires can lead to issues such as the wire snapping or slipping off the rotating shaft. Additionally, while the 3D-printed components are cost-effective, they tend to become fragile when exposed to temperature fluctuations and sunlight in outdoor greenhouse environments. This issue could be addressed with more careful material selection.

According to our observations, the successfully picked fruits were all located in the lower central area of the image frame. In this region, the 2s-FLC appeared particularly effective, with the picking mechanism displaying minimal sway. Adjusting the distribution surface of the fuzzy rules within the 2s-FLC system might yield different results, which warrants further investigation. This harvesting system is optimized for movement along a mounted rail, and the current gripper is specifically designed for handling herbaceous

plants. Most harvesting robot prototypes achieve a picking success rate of around 66%, with an average picking cycle of 33 s per fruit [56]. In contrast, our experimental results show an average picking time of 6.5 s per fruit, with a maximum success rate of 82%, demonstrating the high efficiency of this design. Excluding the arm reset time, the picking time can be further reduced to 5 s, comparable to the single fruit picking time for kiwifruit achieved by Mu et al. [57]. However, due to constantly changing crop backgrounds and lighting conditions, the position of the end effector during picking can vary, affecting the picking success rate [8,42,58]. This variability impacts the overall performance of the picking mechanism. In addition, to improving harvest rates, the non-contact gripping method used in this study minimizes fruit surface damage, enhancing the commercial value of the harvester and the quality of the fruit.

5. Conclusions

The fruit picking mechanism and precision control strategy proposed in this study were initially applied to strawberry harvesting in a hydroponic greenhouse. The cutting gripper, designed to grasp the fruit stem, minimizes surface damage to the strawberries. Three models of ripe strawberries of different sizes were used to validate the effectiveness of the proposed system. The harvesting system achieved a detection accuracy of 90% and a harvesting success rate of 82%, with an average picking time of 6.5 s per strawberry, reduced to 5 s when arm recovery was omitted, enabling the system to potentially pick around 553 strawberries per hour. However, performance is affected by lighting conditions: success rates drop to 32% in early cloudy mornings, while higher success rates are recorded in bright early mornings. Light intensity notably influences picking accuracy, with increased errors in low-light conditions. Future work will include assessing the system with real fruit under natural conditions, broadening image recognition types (e.g., fruit quality inspection), and integrating a spraying system to enhance flexibility.

Author Contributions: Conceptualization, C.-L.C. and C.-C.H.; methodology, C.-L.C.; software, C.-C.H.; verification, C.-C.H.; data management, C.-C.H.; writing—manuscript preparation, C.-L.C. and C.-C.H.; writing—review and editing, C.-L.C.; visualization, C.-L.C.; supervision, C.-L.C.; project management, C.-L.C.; fund acquisition, C.-L.C. All authors have read and agreed to the published version of the manuscript.

Funding: This research was funded by the National Science and Technology Council, grant number NSTC 112-2221-E-020-013; NSTC 113-2221-E-020-018.

Institutional Review Board Statement: Not applicable.

Informed Consent Statement: Not applicable.

Data Availability Statement: Data are contained within the article.

Conflicts of Interest: The authors declare no conflicts of interest.

References

1. Montoya-Cavero, L.E.; de León Torres, R.D.; Gómez-Espinosa, A.; Cabello, J.A.E. Vision systems for harvesting robots: Produce detection and localization. *Comput. Electron. Agric.* **2022**, *192*, 106562. [CrossRef]
2. Botterill, T.; Paulin, S.; Green, R.; Williams, S.; Lin, J.; Saxton, V.; Mills, S.; Chen, X.; Corbett-Davies, S. A robot system for pruning grape vines. *J. Field Robot.* **2017**, *34*, 1100–1122. [CrossRef]
3. Zahid, A.; Mahmud, M.S.; He, L.; Heinemann, P.; Choi, D.; Schupp, J. Technological advancements towards developing a robotic pruner for apple trees: A review. *Comput. Electron. Agric.* **2021**, *189*, 106383. [CrossRef]
4. Bechar, A.; Vigneault, C. Agricultural robots for field operations. Part 2: Operations and systems. *Biosyst. Eng.* **2017**, *153*, 110–128. [CrossRef]
5. Li, K.; Huo, Y.; Liu, Y.; Shi, Y.; He, Z.; Cui, Y. Design of a lightweight robotic arm for kiwifruit pollination. *Comput. Electron. Agric.* **2022**, *198*, 107114. [CrossRef]
6. Zujevs, A.; Osadcuks, V.; Ahrendt, P. Trends in robotic sensor technologies for fruit harvesting: 2010–2015. *Procedia Comput. Sci.* **2015**, *77*, 227–233. [CrossRef]

7. Xiong, Y.; From, P.J.; Isler, V. Design and evaluation of a novel cable-driven gripper with perception capabilities for strawberry picking robots. In Proceedings of the 2018 IEEE International Conference on Robotics and Automation (ICRA), Brisbane, Australia, 21–25 May 2018; pp. 7384–7391. [CrossRef]
8. Williams, H.A.; Jones, M.H.; Nejati, M.; Seabright, M.J.; Bell, J.; Penhall, N.D.; MacDonald, B.A. Robotic kiwifruit harvesting using machine vision, convolutional neural networks, and robotic arms. *Biosyst. Eng.* **2019**, *181*, 140–156. [CrossRef]
9. Ling, X.; Zhao, Y.; Gong, L.; Liu, C.; Wang, T. Dual-arm cooperation and implementation for robotic harvesting of to-matoes using binocular vision. *Robot. Auton. Syst.* **2019**, *114*, 134–143. [CrossRef]
10. Zhang, K.; Lammers, K.; Chu, P.; Li, Z.; Lu, R. System design and control of an apple harvesting robot. *Mechatronics* **2021**, *79*, 102644. [CrossRef]
11. Rahul, K.; Raheman, H.; Paradkar, V. Design and development of a 5R 2DOF parallel robot arm for handling paper pot seedlings in a vegetable transplanter. *Comput. Electron. Agric.* **2019**, *166*, 105014. [CrossRef]
12. Kamandar, M.R.; Massah, J.; Jamzad, M. Design and evaluation of hedge trimmer robot. *Comput. Electron. Agric.* **2022**, *199*, 107065. [CrossRef]
13. Chubb, K.; Berry, D.; Burke, T. Towards an ontology for soft robots: What is soft? *Bioinspir. Biomim.* **2019**, *14*, 063001. [CrossRef]
14. Huang, C.C.; Chang, C.L. Design and implementation of bio-inspired snake bone-armed robot for agricultural irrigation application. *IFAC-PapersOnLine* **2019**, *52*, 98–101. [CrossRef]
15. Chang, C.L.; Shie, J.L. Design and implementation of an actuator for the swing mechanism of a bio-mimosa robot. *J. Chin. Soc. Mech. Eng.* **2013**, *34*, 137–142.
16. Sparrman, B.; du Pasquier, C.; Thomsen, C.; Darbari, S.; Rustom, R.; Laucks, J. Printed silicone pneumatic actuators for soft robotics. *Addit. Manuf.* **2021**, *40*, 101860. [CrossRef]
17. Gariya, N.; Kumar, P. A review on soft materials utilized for the manufacturing of soft robots. *Mater. Today Proc.* **2021**, *46*, 11177–11181. [CrossRef]
18. de Preter, A.; Anthonis, J.; De Baerdemaeker, J. Development of a robot for harvesting strawberries. *IFAC-PapersOnLine* **2018**, *51*, 14–19. [CrossRef]
19. Fan, P.; Yan, B.; Wang, M.; Lei, X.; Liu, Z.; Yang, F. Three-finger grasp planning and experimental analysis of picking patterns for robotic apple harvesting. *Comput. Electron. Agric.* **2021**, *188*, 106353. [CrossRef]
20. Hofer, M.; D'Andrea, R. Design, fabrication, modeling, and control of a fabric-based spherical robotic arm. *Mechatronics* **2020**, *68*, 102369. [CrossRef]
21. Salman, F.; Cui, Y.; Imran, Z.; Liu, F.; Wang, L.; Wu, W. A wireless-controlled 3D printed robotic hand motion system with flex force sensors. *Sens. Actuators A Phys.* **2020**, *309*, 112004. [CrossRef]
22. Li, Z.; Du, R.; Lei, M.C.; Yuan, S.M. Design and analysis of a biomimetic wire-driven robot arm. In Proceedings of the ASME International Mechanical Engineering Congress and Exposition, Denver, CO, USA, 11–17 November 2011; pp. 191–198.
23. Dong, X.; Raffles, M.; Guzman, S.C.; Axinte, D.; Kell, J. Design and analysis of a family of snake arm robots connected by compliant joints. *Mech. Mach. Theory* **2014**, *77*, 73–91. [CrossRef]
24. Li, Z.; Ren, H.; Chiu, P.W.Y.; Du, R.; Yu, H. A novel constrained wire-driven flexible mechanism and its kinematic analysis. *Mech. Mach. Theory* **2016**, *95*, 59–75. [CrossRef]
25. Tang, Y.; Qiu, J.; Zhang, Y.; Wu, D.; Cao, Y.; Zhao, K.; Zhu, L. Optimization strategies of fruit detection to overcome the challenge of unstructured background in field orchard environment: A review. *Precis. Agric.* **2023**, *24*, 1183–1219. [CrossRef]
26. Zhang, Y.; Zhang, K.; Yang, L.; Zhang, D.; Cui, T.; Yu, Y.; Liu, H. Design and simulation experiment of ridge planting strawberry picking manipulator. *Comput. Electron. Agric.* **2023**, *208*, 107690. [CrossRef]
27. Dimeas, F.; Sako, D.V.; Moulianitis, V.C.; Aspragathos, N.A. Design and fuzzy control of a robotic gripper for efficient strawberry harvesting. *Robotica* **2015**, *33*, 1085–1098. [CrossRef]
28. van Herck, L.; Kurtser, P.; Wittemans, L.; Edan, Y. Crop design for improved robotic harvesting: A case study of sweet pepper harvesting. *Biosyst. Eng.* **2020**, *192*, 294–308. [CrossRef]
29. Kaleem, A.; Hussain, S.; Aqib, M.; Cheema, M.J.M.; Saleem, S.R.; Farooq, U. Development challenges of fruit-harvesting robotic arms: A critical review. *AgriEngineering* **2023**, *5*, 2216–2237. [CrossRef]
30. Zhao, Y.; Gong, L.; Liu, C.; Huang, Y. Dual-arm robot design and testing for harvesting tomatoes in a greenhouse. *IFAC-PapersOnLine* **2016**, *49*, 161–165. [CrossRef]
31. Shaw, J.; Cheng, K.Y. Object identification and 3-D position calculation using eye-in-hand single camera for robot gripper. In Proceedings of the International Conference on Industrial Technology, Taipei, Taiwan, 14–17 March 2016; pp. 1622–1625. [CrossRef]
32. Ge, Y.; From, P.J.; Xiong, Y. Multi-view gripper internal sensing for the regression of strawberry ripeness using a mini-convolutional neural network for robotic harvesting. *Comput. Electron. Agric.* **2024**, *216*, 108474. [CrossRef]
33. Hayashi, S.; Shigematsu, K.; Yamamoto, S.; Kobayashi, K.; Kohno, Y.; Kamata, J.; Kurita, M. Evaluation of a strawberry-harvesting robot in a field test. *Biosyst. Eng.* **2010**, *105*, 160–171. [CrossRef]
34. Ge, Y.; Xiong, Y.; From, P.J. Instance segmentation and localization of strawberries in farm conditions for automatic fruit harvesting. *IFAC-PapersOnLine* **2019**, *52*, 294–299. [CrossRef]
35. Sun, T.; Zhang, W.; Miao, Z.; Zhang, Z.; Li, N. Object localization methodology in occluded agricultural environments through deep learning and active sensing. *Comput. Electron. Agric.* **2023**, *212*, 108141. [CrossRef]

36. Perez-Borrero, I.; Marin-Santos, D.; Vasallo-Vazquez, M.J.; Gegundez-Arias, M.E. A new deep-learning strawberry instance segmentation methodology based on a fully convolutional neural network. *Neural Comput. Appl.* **2021**, *33*, 15059–15071. [CrossRef]
37. Tian, Y.; Yang, G.; Wang, Z.; Wang, H.; Li, E.; Liang, Z. Apple detection during different growth stages in orchards using the improved YOLO-V3 model. *Comput. Electron. Agric.* **2019**, *157*, 417–426. [CrossRef]
38. Zhou, X.; Ampatzidis, Y.; Lee, W.S.; Zhou, C.; Agehara, S.; Schueller, J.K. Deep learning-based postharvest strawberry bruise detection under UV and incandescent light. *Comput. Electron. Agric.* **2022**, *202*, 107389. [CrossRef]
39. He, Z.; Karkee, M.; Zhang, Q. Detecting and localizing strawberry centers for robotic harvesting in field environment. *IFAC-PapersOnLine* **2022**, *55*, 30–35. [CrossRef]
40. Eizentals, P.; Oka, K. 3D pose estimation of green pepper fruit for automated harvesting. *Comput. Electron. Agric.* **2016**, *128*, 127–140. [CrossRef]
41. Li, Y.; Wang, W.; Guo, X.; Wang, X.; Liu, Y.; Wang, D. Recognition and positioning of strawberries based on improved YOLOv7 and RGB-D sensing. *Agriculture* **2024**, *14*, 624. [CrossRef]
42. Tang, Y.; Chen, M.; Wang, C.; Luo, L.; Li, J.; Lian, G.; Zou, X. Recognition and localization methods for vision-based fruit picking robots: A review. *Front. Plant Sci.* **2020**, *11*, 510. [CrossRef]
43. Zhang, B.; Xie, Y.; Zhou, J.; Wang, K.; Zhang, Z. State-of-the-art robotic grippers, grasping and control strategies, as well as their applications in agricultural robots: A review. *Comput. Electron. Agric.* **2020**, *177*, 105694. [CrossRef]
44. Han, C.; Lv, J.; Dong, C.; Li, J.; Luo, Y.; Wu, W.; Abdeen, M.A. Classification, advanced technologies, and typical applications of end-effector for fruit and vegetable picking robots. *Agriculture* **2024**, *14*, 1310. [CrossRef]
45. Zadeh, L.A. Fuzzy sets. *Inf. Control* **1965**, *8*, 338–353. [CrossRef]
46. Narendran, V.; Edberg, C.P.L.; Gandhi, G.M. Autonomous robot for e-farming based on fuzzy logic reasoning. *Int. J. Pure Appl. Math.* **2018**, *118*, 3811–3821.
47. Chang, C.L.; Chen, H.W.; Ke, J.Y. Robust guidance and selective spraying based on deep learning for an advanced four-wheeled farming robot. *Agriculture* **2023**, *14*, 57. [CrossRef]
48. Tian, G.; Zhou, J.; Gu, B. Slipping detection and control in gripping fruits and vegetables for agricultural robot. *Int. J. Agric. Biol. Eng.* **2018**, *11*, 45–51. [CrossRef]
49. Liang, X.; Peng, M.; Lu, J.; Qin, C. A visual servo control method for tomato cluster-picking manipulators based on a TS fuzzy neural network. *Trans. ASABE* **2021**, *64*, 529–543. [CrossRef]
50. Li, Z.; Du, R. Design and analysis of a bio-inspired wire-driven multi-section flexible robot. *Int. J. Adv. Robot. Syst.* **2013**, *10*, 209. [CrossRef]
51. Chang, C.L.; Chung, S.C.; Fu, W.L.; Huang, C.C. Artificial intelligence approaches to predict growth, harvest day, and quality of lettuce (*Lactuca sativa* L.) in an IoT-enabled greenhouse system. *Biosyst. Eng.* **2021**, *212*, 77–105. [CrossRef]
52. Bochkovskiy, A.; Wang, C.; Liao, H. YOLOv4: Optimal speed and accuracy of object detection. *arXiv* **2020**, arXiv:2004.10934.
53. Huang, C.C.; Chang, C.L. Design and implementation of wire-driven multi-joint robotic arm. In Proceedings of the 2022 International Conference on Advanced Robotics and Intelligent Systems, Taipei, Taiwan, 24–27 August 2022. [CrossRef]
54. Chang, C.L.; Xie, B.X.; Chung, S.C. Mechanical control with a deep learning method for precise weeding on a farm. *Agriculture* **2021**, *11*, 1049. [CrossRef]
55. Hua, X.; Li, H.; Zeng, J.; Han, C.; Chen, T.; Tang, L.; Luo, Y. A review of target recognition technology for fruit picking robots: From digital image processing to deep learning. *Appl. Sci.* **2023**, *13*, 4160. [CrossRef]
56. Arad, B.; Balendonck, J.; Barth, R.; Ben-Shahar, O.; Edan, Y.; Hellström, T.; Hemming, J.; Kurtser, P.; Ringdahl, O.; Tielen, T.; et al. Development of a sweet pepper harvesting robot. *J. Field Robot.* **2020**, *37*, 1027–1039. [CrossRef]
57. Mu, L.; Cui, G.; Liu, Y.; Cui, Y.; Fu, L.; Gejima, Y. Design and simulation of an integrated end-effector for picking kiwifruit by robot. *Inf. Process. Agric.* **2020**, *7*, 58–71. [CrossRef]
58. Hemming, J.; Ruizendaal, J.; Hofstee, J.W.; van Henten, E.J. Fruit detectability analysis for different camera positions in sweet-pepper. *Sensors* **2014**, *14*, 6032–6044. [CrossRef]

Disclaimer/Publisher's Note: The statements, opinions and data contained in all publications are solely those of the individual author(s) and contributor(s) and not of MDPI and/or the editor(s). MDPI and/or the editor(s) disclaim responsibility for any injury to people or property resulting from any ideas, methods, instructions or products referred to in the content.